

All-chemical $\text{YBa}_2\text{Cu}_3\text{O}_{7-\delta}$ coated conductors with preformed BaHfO_3 and BaZrO_3 nanocrystals on Ni5W technical substrate at the industrial scale

All-chemical $\text{YBa}_2\text{Cu}_3\text{O}_{7-\delta}$ coated conductors with preformed BaHfO_3 and BaZrO_3 nanocrystals on Ni5W technical substrate at the industrial scale

Javier Díez-Sierra^{1,2}, Hannes Rijckaert^{1,*} , Mark Rikel^{2,7}, Jens Hänisch³ , Mario Sadewasser², Lisa Koliotassis², Alexander Meledin^{4,5} , Pedro López-Domínguez¹, Martina Falter², Jan Bennewitz⁶, Michael Bäcker^{2,8} and Isabel Van Driessche¹ 

¹ Department of Chemistry, Ghent University, Krijgslaan 281—S3, 9000 Ghent, Belgium

² Deutsche Nanoschicht GmbH, Heisenbergstr. 16, 53359 Rheinbach, Germany

³ Karlsruhe Institute of Technology, Institute for Technical Physics, Hermann-von-Helmholtz-Platz 1, 76344 Eggenstein-Leopoldshafen, Germany

⁴ RWTH Aachen University, Central Facility for Electron Microscopy, 52074 Aachen, Germany

⁵ Forschungszentrum Jülich GmbH, Ernst Ruska-Centre for Microscopy and Spectroscopy with Electrons (ER-C), 52428 Jülich, Germany

⁶ BASF SE, Advanced Materials and Systems Research, Carl-Bosch-Str. 38, 67056 Ludwigshafen, Germany

E-mail: Hannes.Rijckaert@UGent.be

Abstract

We report a successful fabrication of long-length rolling-assisted biaxially-textured substrate-based coated conductors (CCs) via chemical solution deposition starting from colloidal $\text{YBa}_2\text{Cu}_3\text{O}_{7-\delta}$ (YBCO) solutions containing 5 mol-% preformed BaMO_3 ($M = \text{Hf}, \text{Zr}$) (BMO) nanocrystals. Partial optimization of the existing continuous reel-to-reel YBCO processing via design of experiments approach allowed us to obtain YBCO nanocomposites that retain 80%–90% self-field performance of the pristine CC and show a 10%–40% improvement of in-field critical current, which is only a moderate performance improvement compared to similar films on single-crystal substrates prepared on lab-scale. Based on x-ray diffraction and transmission electron microscopy studies, we attribute this to worsening of the YBCO texture and strong coarsening of BMO nanoparticles, particularly, BaZrO_3 , during processing. Possible process improvements to overcome these effects are discussed.

Keywords: coated conductors, nanocomposite, nanoparticles, vortex pinning, reel-to-reel, chemical solution deposition, superconductor

⁷ Present address: S-Innovations, Nauchnyi proezd, 20, 117246 Moscow, Russia

⁸ Present address: MaTech-Consult GmbH, Plankgasse 58, 50668 Köln, Germany

* Author to whom any correspondence should be addressed.

1. Introduction

To exploit the potential of low-cost high temperature superconductors (HTS) with excellent performance [1], coated conductor (CC) technology was developed based on all-chemical thin films with multilayer architectures (i.e. protective layer/epitaxial REBa₂Cu₃O_{7- δ} (REBCO, RE = rare earth) layer/buffer layers) deposited onto metallic substrates [2]. In the all-chemical route, multilayers are deposited via chemical solution deposition (CSD) technique onto rolling-assisted biaxially-textured substrate (RABiTS). The in-field superconducting performance of pristine YBa₂Cu₃O_{7- δ} (YBCO) layer is often insufficient for applications due to a strong reduction of critical current (I_c) in applied magnetic fields $B = \mu_0 H$ caused by vortex motion [3]. Therefore, artificial pinning centers are incorporated as nano-sized defects in the REBCO matrix to achieve the immobilization of vortices, enhancing in-field I_c as well as its isotropy [4–7]. For CSD-grown REBCO nanocomposites, the pinning centers can be introduced via spontaneous segregation of nanoparticles (*in-situ* approach [8–10]) or starting from preformed nanocrystals (*ex-situ* approach [11, 12]). The latter approach, which starts from colloidal solutions, promises better control of the particle size distribution than the usual method of self-assembled nanoparticles [13–16]. Colloidal single metal oxide MO_2 nanocrystals ($M = \text{Zr}$ and Hf) were used first [13, 17]. Their reaction with Ba^{2+} leads to formation of large BaMO_3 (BMO) nanoparticles in the YBCO matrix. It can be expected that the reactivity of the MO_2 nanocrystals could be avoided by using preformed double metal oxide BMO nanocrystals [18]. We have recently shown that preformed BMO nanocrystals can be introduced in YBCO films on LaAlO_3 substrates without disturbing their epitaxial growth, which leads to an improvement of the pinning capability by a factor of three [19].

The goal of this work is transferring our previous results of the YBCO nanocomposite starting from colloidal YBCO solutions on single-crystal substrates to long-length buffered RABiTS and from the lab scale to the industrial level, i.e. fabrication of long-length YBCO nanocomposite CC via the *ex-situ* approach and by an all-CSD method via a continuous industrial reel-to-reel (RTR) process. Optimization of the already established industrial process led to a 10%–40% in-field I_c increase of BaHfO₃ (BHO)-added YBCO nanocomposite tapes at temperatures between 30 and 77 K. The possibilities of further improvement are discussed based on the microstructure analysis of the nanocomposites.

2. Experimental section

2.1. Synthesis of preformed BMO nanocrystals

BHO and BaZrO₃ (BZO) nanocrystals were synthesized on an industrial scale via a microwave-assisted solvothermal method with the same procedure as described in the patent application WO2020/049019A1 [20] and outlined in the supplementary material. The morphology and size distribution (>150 individual particles counted) of the nanocrystals in the colloidal suspension were studied by transmission electron

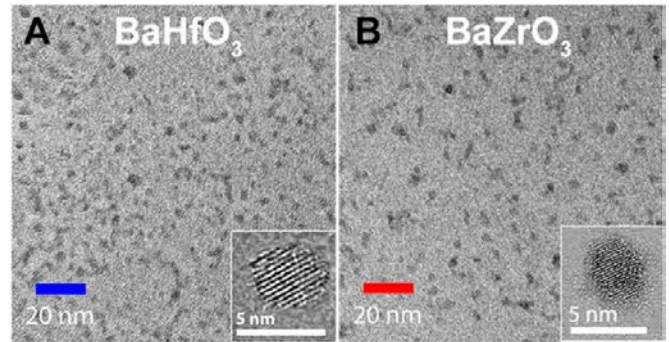


Figure 1. TEM images of agglomeration-free BHO (a) and BZO (b) nanocrystals with average diameters of 4.9 ± 0.6 nm and 4.1 ± 0.5 nm, respectively.

microscopy (TEM, JEOL JEM-2000FS operated at 200 kV), which confirmed the presence of agglomeration-free nanocrystals with average diameters of 4.9 ± 0.6 nm for BHO and 4.1 ± 0.5 nm for BZO, figure 1. These nanocrystals show pseudo-cubic structure and were stabilized with a polyethylene glycol bisphosphonate according to [21], yielding the colloiddally stable and agglomeration-free nanosuspensions in methanol (figure S1 (available online at stacks.iop.org/SUST/34/114001/mmedia)).

2.2. Fabrication of the CCs

The templates used in this work were about 100 m long 10 mm wide CSD-buffered tapes from the standard production of Deutsche Nanoschicht GmbH (D-Nano, Germany), consisting of 60 μm thick Ni-5at% W alloy (Ni5W) RABiTS (>99% Cube within 15° misorientation) coated with 96%–97% epitaxial CSD-La₂Zr₂O₇ (LZO) and CSD-CeO₂ buffer layers [22–24]. YBCO precursor solutions with 69% reduced fluorine content were prepared by dissolving Y-propionate, Ba-trifluoroacetate, and Cu-propionate in an Y:Ba:Cu ratio of 1.3:1.8:3 in methanol (CHROMASOLV, $\geq 99.9\%$ —Sigma-Aldrich) with a total metal ion concentration of 1.1 M. For the colloidal BMO-added YBCO precursor solutions, adequate amounts of nanosuspensions were added to the pristine YBCO precursor solution to obtain a 5 mol-% content of nanocrystals.

Both pristine and colloidal YBCO precursor solutions were deposited on the buffered substrate via slot-die technique using the industrial RTR equipment of D-Nano (see a schematic illustration in supplementary information, figure S3). The layer thickness was adjusted to correspond to 1.50 ± 0.05 μm final YBCO film. After deposition and drying at a temperature of 50 °C to evaporate the solvent (methanol), the tapes were subjected to a three-step thermal treatment (as described in patent application WO2016/150781A1 [25]) to grow the epitaxial YBCO film. Namely, the process consisted in thermal decomposition (pyrolysis) of the dried layer, first heating process (the so-called nucleation step), and a second heating process (growth step). The main parameters of this multistep thermal process (time-temperature profiles, process atmosphere and gas exchange conditions) were optimized by

Table 1. Values of the variables in each level chosen for the central composite design: maximum processing temperature (χ_1, T), water mass flow rate (χ_2, \dot{m}), tape speed (χ_3, v), total pressure (χ_4, P) and oxygen concentration (χ_5, xO_2).

| Variables | $-\alpha_s (-1.61)$ | -1 | 0 | $+1$ | $\alpha_s (1.61)$ |
|---|---------------------|-------------------|-------------|-------------------|-------------------|
| χ_1, T ($^{\circ}\text{C}$) | $T_0 - 32.2$ | $T_0 - 20$ | T_0 | $T_0 + 20$ | $T_0 + 32.2$ |
| χ_2, \dot{m} (g h^{-1}) | $\dot{m}_0 - 161$ | $\dot{m}_0 - 100$ | \dot{m}_0 | $\dot{m}_0 + 100$ | $\dot{m}_0 + 161$ |
| χ_3, v (m h^{-1}) | $v_0 - 8$ | $v_0 - 5$ | v_0 | $v_0 + 5$ | $v_0 + 8$ |
| χ_4, P (mbar) | $P_0 - 3.22$ | $P_0 - 2$ | P_0 | $P_0 + 2$ | $P_0 + 3.22$ |
| χ_5, xO_2 (mol-%) | $x_0 - 1.61$ | $x_0 - 1$ | x_0 | $x_0 + 1$ | $x_0 + 1.61$ |

D-Nano [24, 25] for nanocrystal free YBCO. In this work, standard procedures of D-Nano for 10 mm wide tapes were followed for pristine YBCO, whereas for the nanocrystal-added YBCO, an optimization of the process parameters was needed to reach reasonably high I_c values. This optimization was carried out for BHO-CC only. After YBCO processing, some YBCO tapes were CSD coated with 1 μm thick silver layers on one or both sides.

2.3. Optimization of nanocrystal-added YBCO growth

Only the so-called nucleation step of the multistep thermal process [24–26] was optimized via the design of experiments (DoE) approach [27, 28]. Thus, the self-field critical current, I_c , of the completely converted YBCO on CSD-buffered tapes (after YBCO processing and without a silver coating) was chosen as the response (Y). Two types of DoE were used; namely, a full fractional factorial design (FFD) and a central composite design (CCD). First, a classical FFD experiment was chosen with $k = 3$ variables (maximum processing temperature, total pressure, and oxygen concentration, $2^k = 8$ experiments in total) to determine a suitable center point for the following CCD experiments with $k = 5$ variables (table 1). The CCD allows the independent study of the effect of each variable ($\chi_i, i = 1$ to k) and the interaction between variables through approximating the response by a second-order polynomial:

$$Y = a_0 + \sum_{i=1}^k a_i \chi_i + \sum_{i=1}^k a_{ii} \chi_i^2 + \sum_{i=1}^{k-1} \sum_{j>i}^k a_{ij} \chi_i \chi_j. \quad (1)$$

Five variables for CCD had been identified as potentially affecting the response I_c : maximum processing temperature (χ_1, T), water mass flow rate (χ_2, \dot{m}), tape speed (χ_3, v), total pressure (χ_4, P), and oxygen partial pressure (χ_5, pO_2). A half-fractional factorial design was chosen to reduce the number of experiments from $2^k + 2k +$ center point (43 in total) to $2^{k-1} + 2k +$ center points (29 in total), involving 16 ($=2^{k-1}$) factorial points, 10 ($=2k$) axial points (called ‘star points’ at a distance $\pm\alpha_s = \pm 1.61$ from the center point) and three center points (table 1). Three center points are introduced to assess reproducibility and reduce experimental errors. The CCD experiments were run in random order on 3–5 m long pieces cut from about 100 m long pyrolyzed BHO-added YBCO tapes.

2.4. Electrical characterization

The self-field I_c was measured inductively in liquid nitrogen at 77 K via continuous Hall sensor technique using a THEVA TAPESTAR system over the full tape width for 2–4 m long samples. The corresponding current–voltage curves were measured with a standard four-point technique on representative, 20 cm long defect-free pieces also in liquid nitrogen. The electric field criterion for transport I_c was 1 $\mu\text{V cm}^{-1}$. From these representative pieces, about 5 cm long and 10 mm wide samples containing the voltage taps (10 mm apart from one another) were used for in-field transport measurements at 30 K, 65 K and 77 K in magnetic fields up to 5 T with currents up to 875 A in a custom-made HTS-110 system (Robertson Research Institute, New Zealand [29]). The dependence of I_c on the angle θ between the external magnetic field and the tape normal direction (ND) was measured under maximum Lorentz force configuration (i.e. with the magnetic field perpendicular to the transport current) with a step size of 1° for fields almost parallel to the surface ($\theta = 85^{\circ}$ – 95°) and 5° otherwise.

2.5. Structural and texture characterization

The phase composition and the texture of the YBCO films—after the oxygenation treatment and before the silver coating—were analyzed by XRD using either a three-circle ($2\theta, \omega, \varphi$) Bruker D4 Endeavor diffractometer and a four-circle ($2\theta, \omega, \varphi, \chi$) Bruker D8 Discovery diffractometer with a 2D detector (both with Cu K_{α} radiation). YBCO’s lattice parameter c was assessed from the peak positions of 00ℓ reflections ($\ell = 1$ – 12), and the microstrain ε_c was calculated from the integral breadth of YBCO $K_{\alpha 1}$ 00ℓ peaks following the unmodified Williamson-Hall approach as described by Scardi *et al* [30].

The texture quality of the epitaxial YBCO films was assessed from rocking curve (ω -scan) and φ -scan measurements. For the out-of-plane texture, the full widths at half maximum (FWHM) values ($\Delta\omega_{\text{TD}}$ and $\Delta\omega_{\text{RD}}$) of both the rocking curves around the transverse (TD) and the rolling direction (RD) are reported. At Bruker D4, the rocking curves were measured at the maximum position of the 005 peak, whereas at Bruker D8, it was possible to simultaneously measure the rocking curves of 005, 006 and 007 reflections of YBCO and assess the average as well as the rocking curve of 200 reflection of Ni5W.

The in-plane texture was characterized by the FWHM value ($\Delta\omega_{\text{ND}}$) of the orientation distribution around the ND, which

was assessed from the FWHM ($\Delta\varphi$) values of 113 and (033, 303) φ scans using the relationship derived by Specht *et al* [31]:

$$\Delta\omega_{\text{ND}} = [\Delta\varphi_{hkl}^2 - (\Delta\omega_{\text{RD}} \tan \chi_{hkl} \cos \varphi_{hkl})^2 - (\Delta\omega_{\text{TD}} \tan \chi_{hkl} \sin \varphi_{hkl})^2]^{1/2} \quad (2)$$

where $90^\circ - \chi_{hkl}$ is the sample tilt from the ND and φ_{hkl} is the azimuth with respect to RD.

The epitaxial fraction (EF)—the ratio of epitaxial YBCO to the total amount of material in the film—was assessed by comparing the spatially and 2θ -integrated intensity of the 005 and 006 reflections of the YBCO film with similar data for a standard (i.e. 005 and 006 reflections of a 200 ± 10 nm thick pulsed laser deposited YBCO film) as described in detail by Rikel *et al* [32, 33].

2.6. Microstructural characterization

The microstructure of the films was studied with a C_s -corrected JEOL JEM 2200-FS scanning transmission electron microscopy (STEM) operated at 200 kV with high-angle annular dark-field (HAADF) detector. Cross-sectional lamellae were prepared by focused ion beam in an FEI Nova 600 Nanolab Dual Beam scanning electron microscopy and extracted using the *in-situ* lift-out procedure with an Omniprobe extraction needle. The software *ImageJ* was used to measure the nanoparticle size diameter distribution in the YBCO matrix from several cross-sectional images. Compositional information about the layers was observed via combining HAADF-STEM with energy dispersive x-ray spectroscopy (EDX). Detailed EDX maps were performed on an FEI Titan electron microscope operated at 200 kV acceleration voltage, equipped with an aberration corrector for the probe-forming lens and with a ‘Super-X’ EDX detector [34].

3. Results

3.1. Optimized self-field I_c of nanocrystal-added CCs

Applying the standard thermal treatment of D-Nano on nanocrystal-added YBCO tapes, self-field I_c values at 77 K of 97 ± 5 A for BHO-added and 79 ± 6 A for BZO-added CCs were obtained, which are low compared to the 349 ± 16 A of pristine YBCO CCs. In the preliminary FFD experiments, the I_c was optimized to 240 A for BHO-CC giving new center points different from the D-Nano standard thermal treatment. Using the CCD experiments (table 1), five parameters of the so-called nucleation stage of BHO-CC were optimized in 29 experiments, which yielded samples with I_c from 0 to 265 A, table S1 in supplementary material. The 21 factors (a_i , a_{ii} , and a_{ij}) of the second-order polynomial model (table S2) indicate that maximum temperature (χ_1) and tape speed (χ_3) are the most significant factors with highly non-linear responses. Using this model, the optimal values of the variables leading to the maximum I_c were obtained (table 2).

Applying the optimal conditions of table 2 resulted in improved $I_c = 279$ A of BHO-CC. Afterwards, the 2.5 m

Table 2. The optimal values leading to the maximum I_c response for BHO-CC^a.

| Variables | Optimal condition |
|---|-------------------|
| χ_1, T ($^\circ\text{C}$) | $T_0 - 12.6$ |
| χ_2, \dot{m} (g h^{-1}) | $\dot{m}_0 + 33$ |
| χ_3, v (m h^{-1}) | $v_0 + 6.7$ |
| χ_4, P (mbar) | $P_0 + 4.7$ |
| χ_5, p_{O_2} (mol-%) | x_0 |

^a The table does not present the complete information showing only the tendencies in variation of parameters when BHO nanocrystals are added. We consider this sufficient because for such a complicated process as low fluorine metal-organic deposition, the real data are highly specific to the particular equipment.

long piece of BHO-CC was coated with a silver layer and re-oxygenated. It showed a rather uniform $I_c = 321 \pm 25$ A which is close to the 349 ± 16 A of the pristine CC, figure 2. These optimized conditions were also used to process a BZO-added CC, which yielded a somewhat lower I_c value of 287 ± 13 A.

3.2. Field and angular dependence of the critical current

The field dependencies of I_c and corresponding pinning force densities (F_p), figure 3, show improvement for the optimized BHO-CC at all temperatures, whereas for BZO-CC only at high temperatures (77 K) an improvement is visible.

$I_c(B)$ can be described with three distinct regions: a low-field plateau up to the so-called accommodation field B^* , a power-law dependence $I_c \sim B^{-\alpha}$ at medium fields, and a rapid decrease of I_c towards the irreversibility field B_{irr} . At 30 K, only the power-law region was observable due to limitations in transport current and magnetic field. The data on accommodation field B^* (determined as $I_c(B^*) = 0.9 \cdot I_{c0}$) and the exponent α of the power law region assessed from the most linear (best χ^2) portion in the double logarithmic plots of figure 3(a) are presented in table 3.

Fitting the F_p curves normalized to $b = B/B_{\text{max}}$ rather than B/B_{irr} , where B_{max} is the field at which F_p is maximum, with a single generalized Dew-Hughes function $F_p \sim (p/q)^q \times b^p(((p+q)/p) - b)^q$ yielded p values in the range 0.45–0.6, i.e. $p \sim 0.5$ (table S3 in supplementary material) taking into account the extra low-field contribution and missing high-field data. The q values are in most cases unphysically large due to missing data near B_{irr} and overestimated I_c values due to large creep effects (small n values). Only for BHO-CC at 77 K the analysis yielded a reasonable value $q = 2.7$, i.e. ~ 2 suggesting that the main pinning contribution can be related to surface pinning with $(p, q) = (0.5, 2)$. Comparison of such a test function with the data for BHO-CC is shown in logarithmic plot of figure 4. The additional pinning component at low fields, marked with an arrow, is clearly recognizable as deviation from the Dew-Hughes dependence with $(p, q) = (0.5, 2)$.

The trend of the irreversibility fields has been estimated by the Kramer field, i.e. by a linear extrapolation in medium-to-high fields of the Kramer function $J_c^{0.5} B^{0.25}$ to zero, table 4.

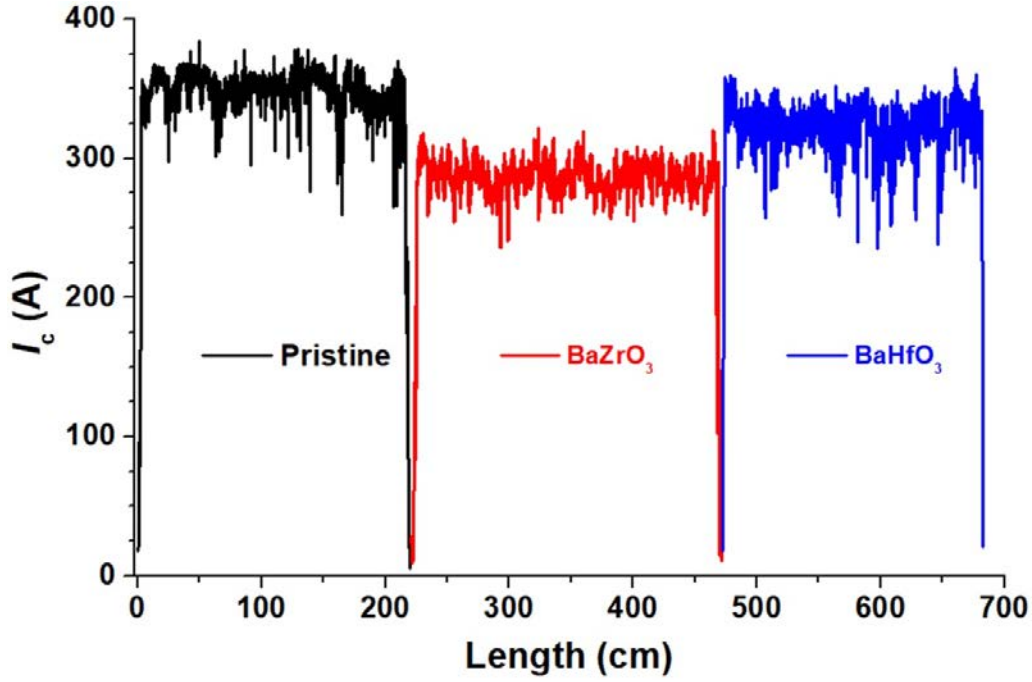


Figure 2. The inductive self-field I_c measured along 2.5 m long pieces of pristine CC, BHO-CC, and BZO-CC after silver coating and re-oxygenation.

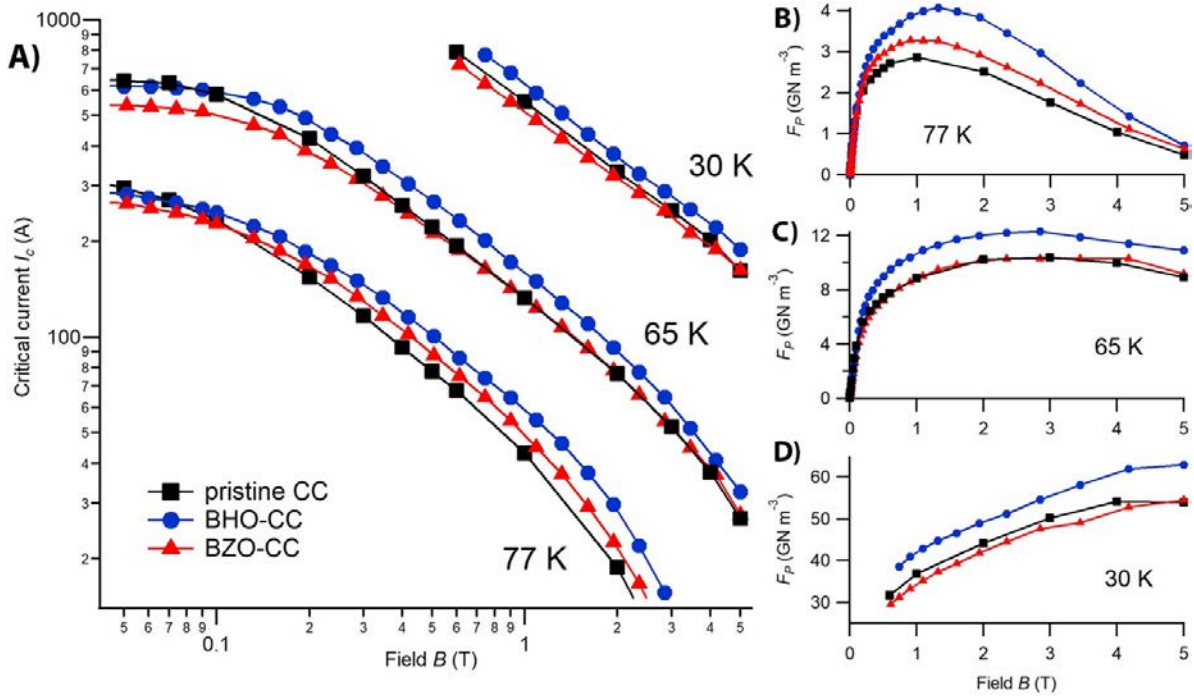


Figure 3. (a) Field dependence of I_c at 77, 65 and 30 K (at 30 K, the measurements were done only in magnetic fields $H > 0.7$ T due to limitations of the current source). Pinning force density versus magnetic field in linear scale, at (b) 77 K, (c) 65 K and (e) 30 K.

The same trend is visible in the $I_c = 10$ A data points in figure 3(a).

The dependence of the transport I_c on the angle θ between the direction of magnetic field and the tape ND at 77 and 65 K, figure 5, shows a strong decrease in the I_c anisotropy

$I_c(B||ab)/I_c(B||c)$ of the nanocomposites (~ 2) compared to the pristine sample (~ 3), table 4. The BZO-CC sample shows a lower I_c in the whole angular range. The ab -peak for the nanocomposite films is somewhat broader than for the pristine sample.

Table 3. Accommodation field B^* and power-law exponent α extracted from $I_c(B)$, figure 3(a), in the given field range. The α values were extracted in the most linear region. The error bars are ~ 3 mT for H^* and $\sim 0.01, 0.007$, and 0.005 for α at 77 K, 65 K, and 30 K, respectively.

| Sample | 77 K | | 65 K | | 30 K |
|----------|---------------|-------------------------|---------------|-------------------------|-------------------------|
| | B^* (mT) | α (0.3–0.9 T) | B^* (mT) | α (0.4–1.6 T) | α (0.7–4.2 T) |
| Pristine | 45 | 0.78 | 90 | 0.735 | 0.72 |
| BHO-CC | 75 | 0.75 | 130 | 0.76 | 0.74 |
| BZO-CC | 60 | 0.78 | 110 | 0.72 | 0.70 |

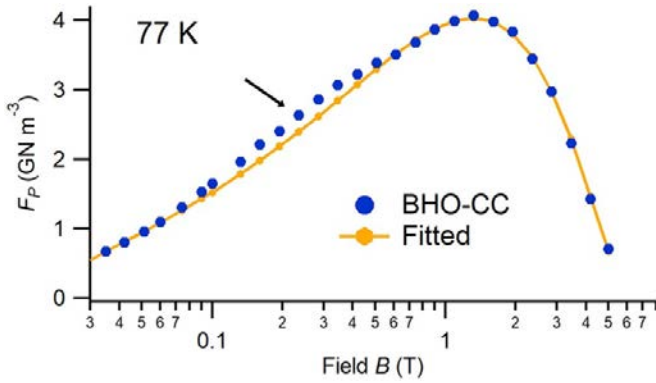


Figure 4. Pinning force density of BHO-CC versus magnetic field at 77 K in logarithmic scale with fitted curve.

3.3. Structural investigation

3.3.1. Phase composition. The XRD θ - 2θ scans of all three CC samples, figure 6, are dominated by the $00l$ reflections of YBCO as well as the peaks corresponding to the Ni5W substrate and the LZO buffer layer. Among the lines with smaller intensity, we first mention (013, 103, 110) peaks ($2\theta = 32.5^\circ$ – 32.8°) corresponding to randomly oriented YBCO and major lines of NiWO_4 and NiO . Other lines can be attributed to Y_2O_3 , $\text{Y}_2\text{Cu}_2\text{O}_5$, $\text{Ba}(\text{O},\text{F})_2$, BHO/BZO, and $\text{Y}_2\text{Ba}_4\text{Cu}_7\text{O}_{15}$ (Y-247). The presence of these secondary phases is confirmed by STEM-EDX analysis (see below). Figure 7 shows the portions of measured 2D patterns that partly illustrate the epitaxial (out-of-plane) relationships between YBCO and other phases. It shows that Y_2O_3 particles are present in the pristine YBCO CC both as textured ones (a short bright arc on the 400 ring smaller than the 400 arc of LZO in the 2D-pattern and strong 400 reflection in the 1D-XRD pattern) and, possibly, as randomly oriented ones (a continuous 222 ring in the 2D pattern and small intensity 222 peak in the 1D XRD pattern next to 222 peak of LZO).

It is also clear from figure 7 that the out-of-plane texture is almost the same for YBCO, Y-247 phase and Y_2O_3 and looks sharper than that of LZO (see also table 6 below). In the BHO-CC and BZO-CC, only continuous and uniform 110 and 200 rings of BHO and BZO are seen suggesting that BHO and BZO nanoparticles are mostly randomly oriented. The most pronounced difference to the pattern of the pristine sample is the strong reduction in intensities of Y_2O_3 peaks ($2\theta \approx 29^\circ$,

34° and 49°) in the patterns of the nanocomposite CCs. The amount of random YBCO is almost unaffected by the addition of BHO and BZO (013,103, 110 peaks almost the same), but the number of ab -grains slightly increases from $<0.1\%$ of 006 in the pristine CC to 0.15% (BHO-CC) and 0.3% (BZO-CC). The amounts of Y-247 and $\text{Ba}(\text{O},\text{F})_2$ are lower in the BHO-CC and BZO-CC than in the pristine CC.

3.3.2. Lattice parameter, microstrain, texture characterization and EF of Y-123 phase. The incorporation of BHO or BZO nanocrystals in the YBCO matrix results in a significant increase in the YBCO lattice parameter c , a rather moderate change in its microstrain ϵ_c , and no change (within the error) in the average crystallite size L_0 along the c -axis, table 5. The lattice parameter c is sensitive to the oxygen content in $\text{YBa}_2\text{Cu}_3\text{O}_{7-\delta}$ (see, e.g. [36]), and the microstrain ϵ_c can be affected by the homogeneity in oxygen distribution within the YBCO layer. To check to what extent these effects may contribute to the difference in c and ϵ_c , all three samples were post-annealed in 1 bar pure oxygen at 285°C . At this temperature, the oxygenation is sluggish (particularly, in BHO-CC and BZO-CC [37]) and usual cooling rates $\sim 1^\circ\text{C s}^{-1}$ fully fix the oxygen distribution in the YBCO matrix. These experiments revealed no changes in c and ϵ_c with increasing oxygenation time from 16 to 110 h, suggesting that the differences in c and ϵ_c reported in table 5 are due to the addition of nanocrystals.

In BHO-CC, the out-of-plane texture $\Delta\omega$ of the YBCO layer is $12 \pm 2\%$ worse than in the pristine CC, whereas the in-plane texture is not affected (table 6). In BZO-CC, $\Delta\omega$ is also worse than in the pristine CC, but the effect is anisotropic ($25 \pm 2\%$ for $\Delta\omega_{\text{TD}}$ and $7 \pm 2\%$ for $\Delta\omega_{\text{RD}}$). An important difference between BHO-CC and BZO-CC is a significantly worse in-plane texture in the BZO-CC of $47 \pm 6\%$. Despite of the worse texture, the EF in the nanocrystal-added CCs is within the error the same as in the pristine CC.

The texture characteristics of Ni5W substrate and LZO buffer layer measured on the same samples and corrected for absorption effects are also shown in table 6. Compared to the LZO template, the out-of-plane texture of YBCO is improved by $\sim 25\%$ in the pristine CC and by $\sim 5\%$ – 20% in the BHO-CC and BZO-CC; the in-plane texture is the same as in LZO (pristine CC and BHO-CC) or worse (BZO-CC). It is important to note a rather high sample-to-sample irreproducibility (3% – 5%) in $\Delta\omega_{\text{RD}}$ and $\Delta\omega_{\text{ND}}$ values for nanocrystal-added YBCO CCs compared to $<1.5\%$ scatter in $\Delta\omega$ for the template. It is, thus, likely that the larger scatter in $\Delta\omega_{\text{RD}}$ and $\Delta\omega_{\text{ND}}$ reported in table 6 is due to the addition of BHO and BZO nanocrystals.

3.3.3. Nanocomposite microstructure. As observed in HAADF-STEM images, the pristine CC (figures 8(a)–(c)) contains ~ 25 vol.% secondary phase particles in the whole YBCO matrix, which is roughly consistent with the EF ~ 75 (wt) % from XRD (table 6), as the mass densities of major secondary phases are rather similar and the errors in both methods are $\sim 5\%$. The secondary phase particles and pores are non-uniformly distributed across the film thickness. The

Table 4. B^{\max} and F_p^{\max} (figure 4), Kramer field B_k , and I_c anisotropy (figure 5) at 77 K and 65 K.

| Sample | B^{\max} (T) | | F_p^{\max} (GN m ⁻³) | | B_k (T) | $I_c(\theta = 90^\circ)/I_c(\theta = 0^\circ)$ | |
|----------|----------------|------|------------------------------------|------|-----------|--|------|
| | 77 K | 65 K | 77 K | 65 K | 77 K | 77 K | 65 K |
| Pristine | 1 | 3.0 | 2.9 | 10.4 | 5.5 | 3.0 | 2.9 |
| BHO-CC | 1.1 | 2.85 | 4.1 | 10.4 | 6.5 | 2.0 | 2.0 |
| BZO-CC | 1.3 | 2.85 | 3.3 | 12.3 | 5.8 | 2.1 | 2.1 |

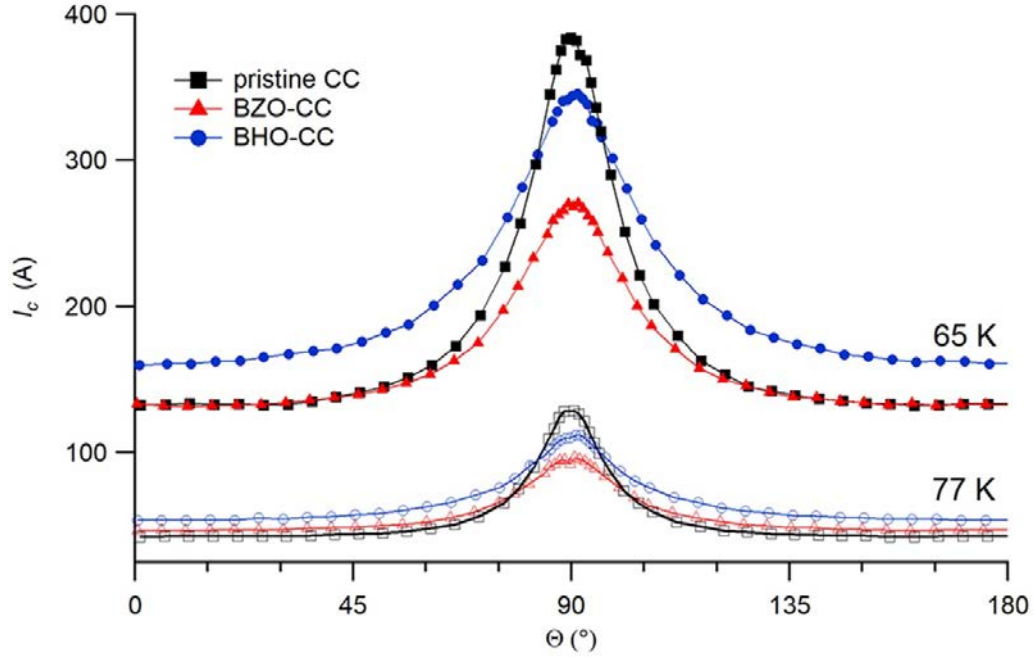


Figure 5. Angular dependence of I_c in an external magnetic field of 1 T at 77 and 65 K.

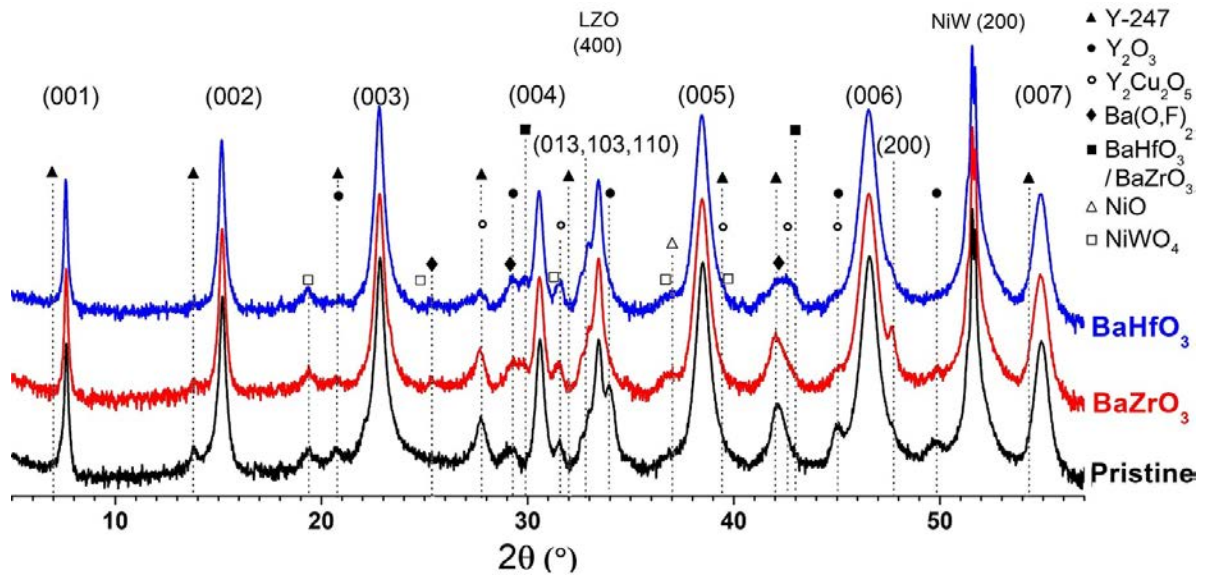


Figure 6. θ - 2θ scan (in logarithmic intensity scale) for the pristine CC, BHO-CC, and BZO-CC. Indexing of peaks is based on the data from [35] for Y-247 and from Powder diffraction file (PDF) for Ba(O,F)₂ (PDF 85-1341), Y₂O₃ (PDF 74-0553), Y₂Cu₂O₅ (PDF 78-2100), NiWO₄ (PDF 72-0480), NiO (PDF 89-7130).

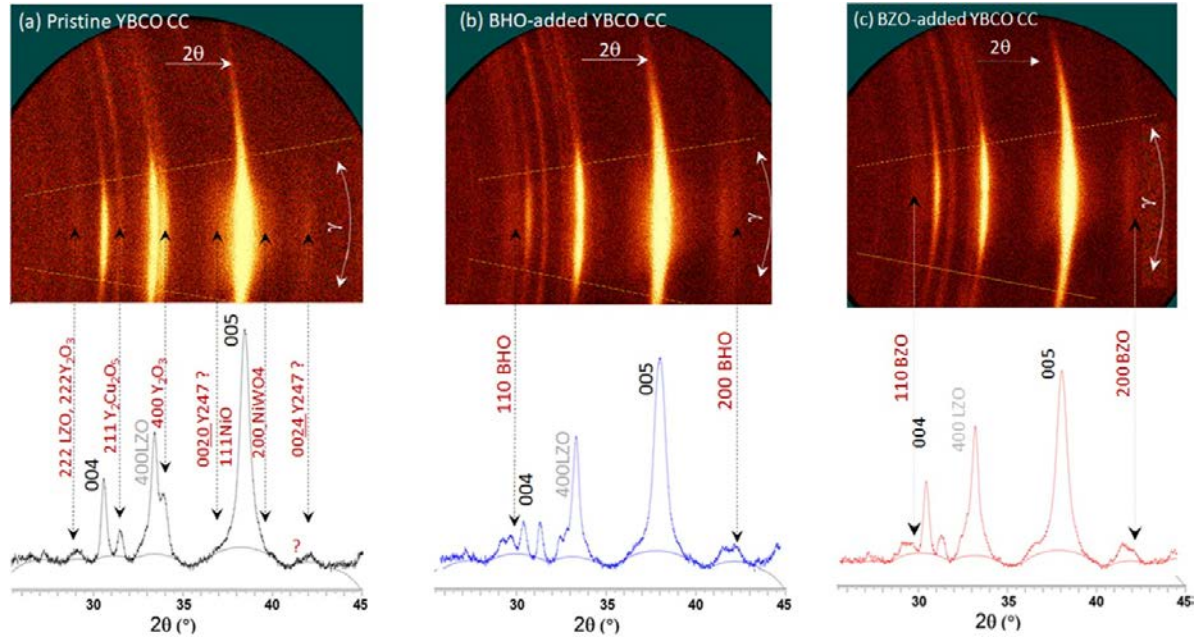


Figure 7. 2D XRD patterns of (a) pristine CC, (b) BHO-CC, (c) BZO-CC and corresponding 1D patterns (in logarithmic intensity scale) obtained by integration of 2D patterns over azimuthal angle γ . The patterns illustrate presence of biaxially textured and possibly randomly oriented Y_2O_3 . Dashed lines in the 2D patterns are drawn to illustrate epitaxial (out-of-plane) relationships between YBCO and other phases.

Table 5. YBCO lattice parameter c , microstrain (ε_c) and the crystallite size L_0 along the c -axis assessed from line broadening effects, of pristine and nanocrystal-added YBCO CCs (numbers in parentheses show the error in the last digit). The data represent average values of at least three measurements.

| | c (Å) | ε_c (%) | L_0 (nm) |
|----------|-------------|---------------------|------------|
| Pristine | 11.7115 (8) | 0.389 (7) | 250 (40) |
| BHO | 11.7232 (8) | 0.449 (5) | 190 (30) |
| BZO | 11.7220 (5) | 0.434 (11) | 210 (40) |

Table 6. Out-of-plane ($\Delta\omega_{TD}$ and $\Delta\omega_{RD}$), and in-plane ($\Delta\omega_{ND}$) texture sharpness (FWHM values), and epitaxial fraction (EF) of pristine and nanocrystal-added YBCO CCs, underlying buffer (LZO/CeO₂) and Ni5W (numbers in parentheses show the error in the last digit(s)). The data represent average values of at least three measurements.

| | $\Delta\omega_{TD}$ (°) | $\Delta\omega_{RD}$ (°) | $\Delta\omega_{ND}$ (°) | EF (%) |
|----------------------|-------------------------|-------------------------|-------------------------|-----------------------|
| Pristine CC | 3.83 (2) | 6.14 (3) | 4.02 (7) | 77 (5) |
| BHO-CC | 4.25 (7) | 7.00 (20) | 4.00 (20) | 73 (4) |
| BZO-CC | 4.81 (6) | 6.54 (11) | 5.90 (20) | 70 (3) |
| LZO/CeO ₂ | 5.12 (7) | 8.15 (11) | 4.08 (7) | 97 (1) ^a |
| Ni5W | 5.20 (7) | 8.80 (16) | 3.36 (12) | 99.8 (1) ^b |

EBSD results: ^a % Cube-indexed;

^b % Cube oriented (<15° misorientation from ND).

particles are bigger in the upper part (~100 nm average diameter) than in the lower part (~50 nm) of the YBCO film. Some porosity (~5%) is present throughout the YBCO film (again especially in the upper part). Higher-magnification

images (figures 8(b) and (c)) show that the secondary phase particles are surrounded by planar defects. The EDX maps of the pristine CC (figure 9(a)) show presence of Y_2O_3 (marked with dashed line). $Ba(O,F)_2$ and $Y_2Cu_2O_5$ are also observed via detailed EDX maps in figure S4. Y-247 inclusions of up to 300 nm in diameter were also seen particularly in the upper parts of the film as identified by the change in lattice spacing observed in the HAADF-STEM image (figure S5). Thus, the results of TEM phase analysis are qualitatively consistent with the results of XRD studies (figures 6 and 7).

The HAADF-STEM images and EDX maps for BHO-CC and BZO-CC also show the results consistent with the XRD data on phase composition. Y_2O_3 is not observed in the EDX maps (figures 9(b) and (c)) of nanocrystal-added CCs. Both BHO-CC and BZO-CC have a noticeably smaller amount of $Ba(O,F)_2$ than the pristine CC while the amount of $Y_2Cu_2O_5$ is similar in all films.

Absence of Y_2O_3 particles in BMO-CCs indicates their interaction with BMO. The detailed EDX maps have been done (figure S6). An example for BZO-CC is shown in figure 10. Line scans across the Zr-rich particles clearly show that Y is dissolved in BZO nanoparticles.

In both BHO-CC and BZO-CC, the BMO nanoparticles are uniformly distributed without any sign of ordering, but significant coarsening is observed with the average particle diameter $\langle d \rangle$ increased to 15 nm for BHO and 17 nm for BZO, both with a mean square deviation $\sigma_d = 5$ nm (cf figure 11).

Planar defects (i.e. stacking faults, SFs) can be seen in all three CCs (figures 8(c), (f), and (i)), where SFs are of different length, mostly of 10–30 nm, rarely up to 250 nm.

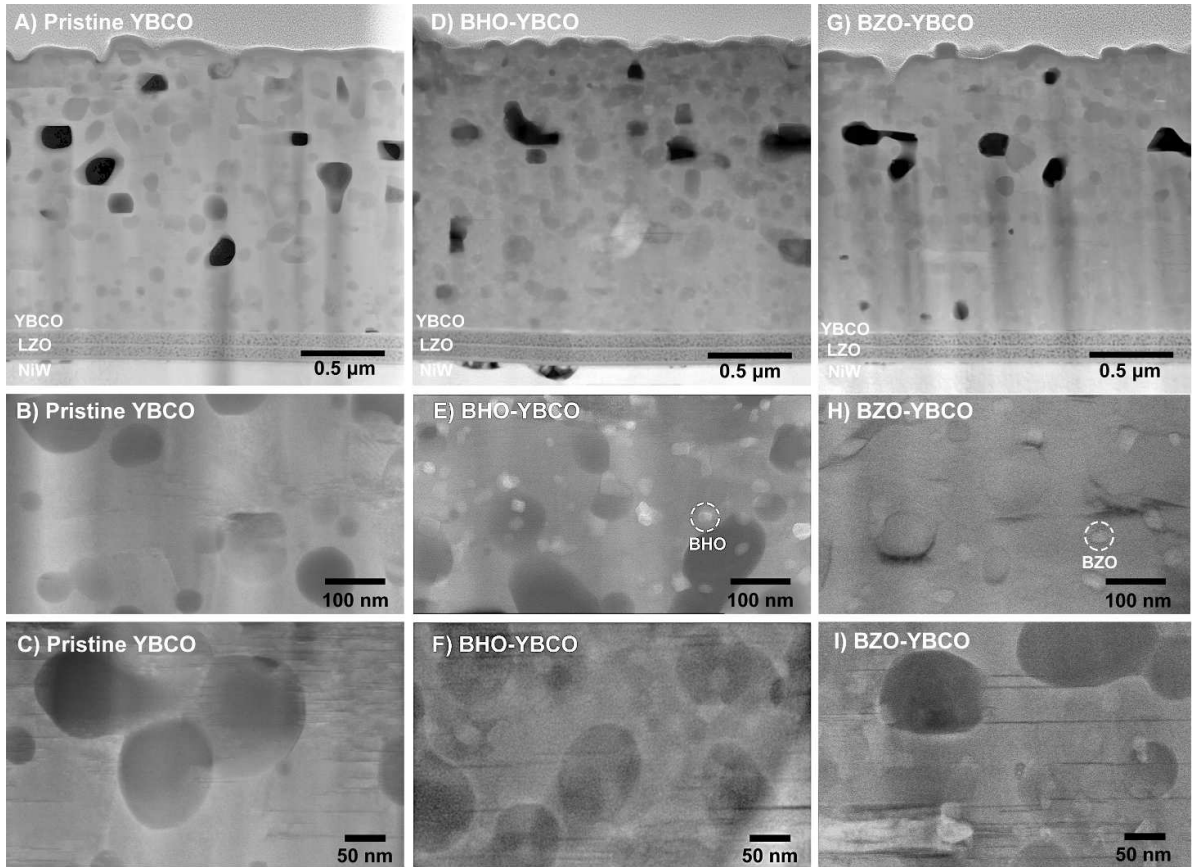


Figure 8. HAADF-STEM images of pristine CC (a)–(c), BHO-CC (d)–(f), and BZO-CC (g)–(i). The nanocrystal-added CCs show a homogeneous distribution of nanoparticles. A similar amount of secondary phase particles and pores are visible in all the CCs, being more frequent in the upper half of the CCs, as well as a high concentration of planar defects.

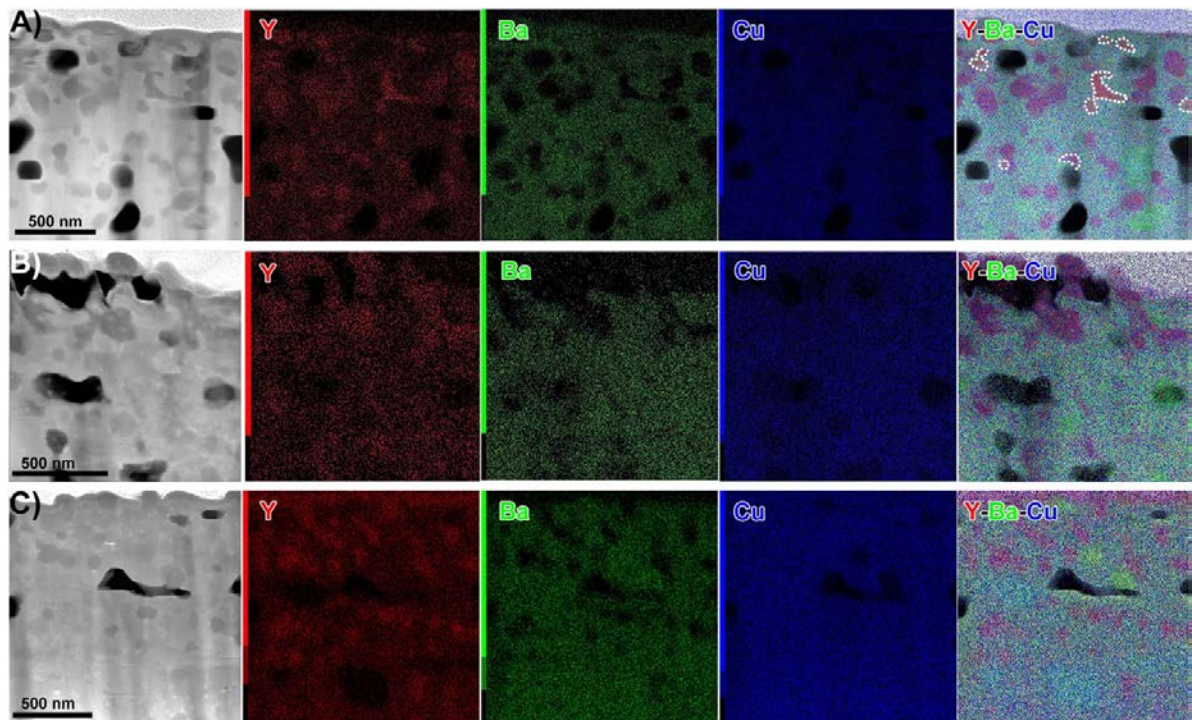


Figure 9. STEM images and corresponding elemental maps, of (a) pristine CC, (b) BHO-CC and (c) BZO-CC obtained via EDX mapping. The color code is red for Y, green for Ba, and blue for Cu.

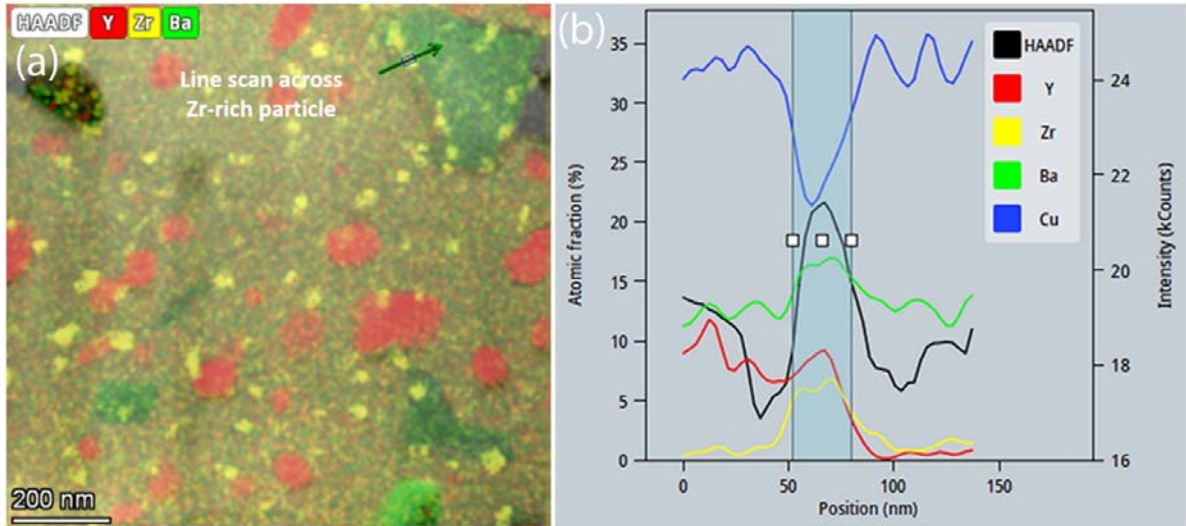


Figure 10. (a) Composite image of HAADF-STEM and elemental Y, Zr, and Ba EDX maps of a cross-sectional BZO-CC; (b) EDX line profile of Y, Zr, Ba, and Cu from the line scan across Zr-rich particles. No Y signal drop is observed, showing a clear evidence of Y in the Zr-rich particles. Ba concentration is not equal to Y because of overlapping volume and quantification error.

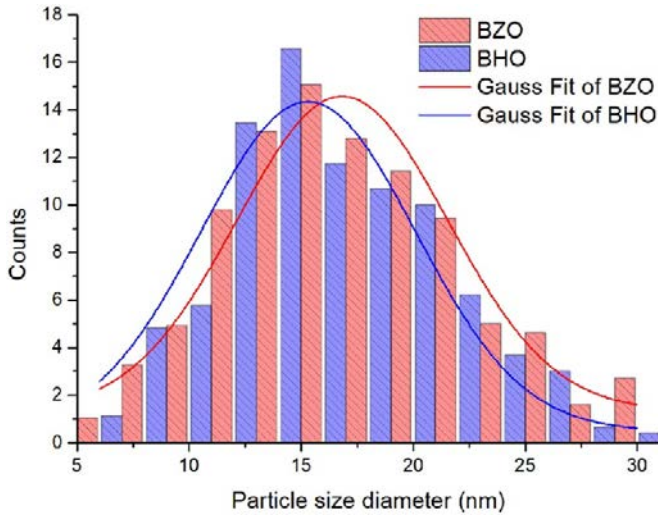


Figure 11. Size distribution of nanoparticles in BZO-CC and BHO-CC measured from HAADF-STEM cross-sectional images. BHO nanoparticles have an average diameter $\langle d \rangle$ of 15 nm and BZO nanoparticle have $\langle d \rangle = 17$ nm, both with standard deviation $\sigma = 5$ nm.

4. Discussion

This work aimed at transferring the fabrication of all-CSD YBCO nanocomposites starting from colloidal precursor solutions from single-crystal substrates to long-length buffered RABiTS and from the lab scale to the industrial level. Optimizing the process parameters of only the nucleation step, we were able to reach the self-field I_c (77 K) that constitutes $>90\%$ (BHO-CC) and $>80\%$ (BZO-CC) of the pristine-CC I_c values. We stress that the difference between the effects of BZO and BHO nanocrystal additions may not be intrinsic but stem from the fact that the optimization was done for the BHO-CC, and the process parameters thus obtained were also used for

the BZO-CC. In general, we may conclude that the optimization strategy chosen based on the earlier results [26, 38] was correct.

On the other hand, the positive effects of adding nanocrystals are much less pronounced than in the case of single-crystal substrates. In our studies of YBCO nanocomposite films on LaAlO_3 [19], the observed $J_c(77, sf)$ were 10% higher in both BHO- and BZO-added YBCO films, and in high fields (>1 T) J_c increased by a factor of three (BHO-added) and two (BZO-added). In the current study, BHO-CC and BZO-CC show a rather moderate increase (~ 40 and 20%) in I_c at 77 K and high fields (>1 T), which becomes less pronounced (20 and 10% in BHO-CC) or even disappears (in BZO-CC) at 65 K and 30 K. Below we discuss the possible reasons for such a modest improvement and possible ways to enhance these positive effects.

4.1. Non-optimized pinning landscape

The processing of the pristine CC and, hence, its microstructure were already optimized with respect to self-field performance at 77 K [24, 25]. Because of the overall nonstoichiometric $\text{Y}_{1.3}\text{Ba}_{1.8}\text{Cu}_{3.0}\text{O}_x$ composition and unfinished reaction (presence of $\text{Ba}(\text{O},\text{F})_2$), it contains rather small (50–100 nm) secondary phase particles (Y_2O_3 and $\text{Y}_2\text{Cu}_2\text{O}_5$) and a rather large density of SFs (figure 8). These defects are possibly the major reason why the addition of 5 mol-% BHO or BZO nanocrystals gives smaller effects on the CC templates than on LaAlO_3 [19]. Indeed, the microstrain $\varepsilon \approx 0.39\%$ in the pristine YBCO-CC is already rather large (compared to $\approx 0.08\%$ in the pristine YBCO on LaAlO_3) and only slightly increases to $\varepsilon \approx 0.45\%$ in BHO-CC and BZO-CC (table 5).

The accommodation field at 77 K of the pristine CC, $B^* = 45 \pm 3$ mT (table 3), is more than one order of magnitude larger than that of the pristine YBCO on LaAlO_3 and twice as large as in 5 mol-% BHO-added YBCO on LaAlO_3 . Adding

Table 7. Summary of the average size diameter of the nanocrystals in the colloidal solution and the particles in YBCO matrix on Ni5W and LaAlO₃ substrates and its calculated coarsening factor.

| BZO | YBCO on Ni5W | | YBCO on LaAlO ₃ [19] | |
|--------------|--------------|--------------|---------------------------------|--------------|
| | BHO | BZO | BHO | |
| Nanocrystals | 4.1 ± 0.6 nm | 4.9 ± 0.5 nm | 3.3 ± 0.4 nm | 2.9 ± 0.4 nm |
| Particles | 17 ± 5 nm | 15 ± 5 nm | 10 ± 6 nm | 7 ± 4 nm |

5 mol-% of nanocrystals (2.2 vol-% BZO or 1.8 vol-% BHO) increases B^* (77 K) suggesting further increase in the density of pins favorable in the low-field range. This is also observable by the additional pinning component in $F_p(B)$ at around 0.3 T, recognizable as shoulder to the main F_p component and most prominent at 77 K for BHO-CC (figure 4).

Despite of the improved pinning in the low-field range, the *self-field* I_c of BMO-added CC are noticeably smaller than in the pristine CC, which cannot be related to smaller T_c (according to [37], T_c of fully oxygenated BHO-CC is higher than that of pristine CC) and most likely is due to the worse texture of BHO-CC and BZO-CC (table 6).

The data on the power law exponent α (table 4) suggest that the BHO and BZO nanoparticles themselves are not the only nor dominant contributors to pinning even in the medium field range. Indeed, all α values for our samples are in the range 0.70–0.78 independently of the presence of nanoparticles. According to simulation results by Willa *et al* [39], in case the nanoparticles were the dominant pinning centers, the exponent α would depend only on the volume fraction of nanoparticles slightly larger than the coherence length ξ , and for the volume fraction of $\sim 2\%$ (i.e. 5 mol-%), one would anticipate a much smaller value $\alpha \sim 0.37$. Note that in 5 mol-% BHO- and BZO-added YBCO films on LaAlO₃ substrates, we observed $\alpha = 0.33$ and 0.38 versus $\alpha = 0.53$ in the pristine films [19].

The $F_p(B)$ data further suggest that the major contribution comes from surface pinning (see figures 3(b)–(d), figure 4 and corresponding discussion). Thus, the pinning behavior in our tape samples is determined by a more complex pinning landscape than by the nanoparticles. Coarsening of nanoparticles during processing is the most likely reason for their low efficiency as pinning centers.

4.2. Evolution of nanoparticles during RTR processing

According to the TEM studies (figure 8), the BHO and BZO nanoparticles remain homogeneously distributed but become coarser during thermal processing (figure 11). The average diameters $\langle d \rangle$ of BHO (15 nm) and BZO (17 nm) are about twice as large as in the lab-scale YBCO films on LaAlO₃ substrates [19], table 7.

Thus, for industrial processing, the nucleation and growth stages of which are inevitably longer than for the lab scale processes, at least because of a factor of five larger YBCO film thickness, using preformed BHO and BZO nanocrystals does not solve the problem of their stability. First, BHO and BZO nanoparticles in the YBCO matrix may react with Y₂O₃, as suggested for PLD-YBCO (PLD, pulsed laser deposition)

[40, 41] and MOCVD-(Gd,Y)BCO films [42] (MOCVD, metal-organic chemical vapor deposition). Such an interaction should result in dissolution of Y₂O₃ in BZO and BHO, where yttrium substitutes up to 25 mol-% Zr or Hf [43, 44]. The strong reduction in the amount of Y₂O₃ in BHO-CC and BZO-CC detected by both XRD (figures 6 and 7) and TEM/EDX (figures 8 and 9) and detailed EDX maps (figure 10) strongly support this interpretation.

Just an interaction of BaMO₃ ($M = \text{Hf, Zr}$) with Y₂O₃ should cause an increase in the nanoparticle volume as is clear from the reaction formula $\text{BaMO}_3 + 0.5x \text{Y}_2\text{O}_3 + x \text{BaO} = (1+x) \text{Ba}(M_{1-x}\text{Y}_x)\text{O}_{3-2x}$, i.e. a 25% increase for the maximum substitution of $x = 0.25$ [43, 44]. It may also affect the surface energy of the nanoparticles and the elastic energy and, hence, the driving force for particle coalescence.

It is known that Y substitution for Zr in BZO results in an essential (up to 1%) increase in the BZO lattice parameter [45], which may lead to a larger stress associated with nanoparticles. Our data on lattice parameter c (table 5) are consistent with this hypothesis. Indeed, compared to the pristine tape, BHO- and BZO-CCs have an increased lattice parameter c , which can be fully related to the additional stress associated with BHO and BZO addition [37, 41]. In our earlier study of 5 mol-% BHO- and BZO-added to stoichiometric (Y:Ba:Cu = 1:2:3) YBCO on LaAlO₃ substrates [17], no reaction between BMO and Y₂O₃ was observed, and the change of the stress state characterized by an increase in the lattice parameter c was a factor of 3 smaller ($\Delta c \approx 0.003 \text{ \AA}$ vs 0.011 \AA). It should be noted that the difference in the lattice parameters c may originate from the difference in coherency of nanoparticles to the YBCO matrix (in PLD-YBCO, where the nanoparticles are mostly coherent to the matrix, $\Delta c = 0.042 \text{ \AA}$ for 5 mol-% BHO addition [41]). However, the fact that 2D XRD patterns (figure 7) show almost uniform 111 and 200 rings of BHO and BZO suggests that this mechanism is unlikely.

The reaction with Y₂O₃ alone cannot explain coarsening of BHO and BZO nanoparticles that requires also mass transfer of other elements. Though, no data on Hf and Zr substitution in YBCO are known, even tiny solubilities are sufficient for mass transfer. Thus, coarsening of fine particles via Ostwald ripening can be anticipated, particularly, if treatment involves partial melting, which is the case for CSD-YBCO processing [46]. Kinetics of Ostwald ripening under isothermal conditions are given by the relation $\langle d \rangle^3(t) - \langle d \rangle^3(0) = Kt$ where $\langle d \rangle$ is the average diameter and the rate constant K is determined by the mass transfer of limiting element [47]. As Y and Ba are abundant in the YBCO matrix, it is natural to consider the mass transfer of Hf or Zr as the limiting factor. The processing conditions for BHO-CC and BZO-CC were the same in this study;

then, it follows for the data of table 7 that the rate constant K in BZO-CC and BHO-CC Zr differ by $50 \pm 15\%$. Qualitatively similar conclusion can be drawn from the data for BHO- and BZO-added YBCO on LaAlO_3 , table 7. Li *et al* [18] also observed coarsening of BMO ($M = \text{Hf}$ and Zr) preformed nanoparticles when processing YBCO-20 mol-% BMO nanocomposites on LaAlO_3 single-crystal substrates with a 25–50 nm thick seed pristine YBCO layer. They did not report any difference in the coarsening rates of BZO and BHO, but the TEM images presented in their paper (figure 5 in [18]) are consistent with our conclusion. They also showed that coarsening of BMO nanoparticles can be suppressed by reducing the reaction time, but in expense of worsening the in-plane texture.

4.3. Paths for improving performance of BMO-added CSD-YBCO

The major conclusion from the above analysis is that strong coarsening of BMO particles during CSD processing is the most likely reason for low efficiency of BMO additions as pinning centers. The in-field performance can be improved if the size of BMO and secondary phase particles are in the order of the superconducting coherence length (2 – 4 nm for YBCO at 77 K) and agglomeration-free (to reach a higher number density of defects in YBCO matrix) [48]. So, understanding the mechanism and kinetics of coarsening are necessary to better control low particle size. However, certain receipts can be formulated based on the available data. Our data suggest that coarsening at least partly stems from interaction of BMO with Y_2O_3 . The reaction can be suppressed by adding yttrium precursor during the microwave synthesis of the preformed nanocrystals leading to Y^{3+} -doped BMO nanocrystals. It is also clear that a simultaneous optimization of yttrium content in the pristine YBCO precursor solution is necessary to make addition of BMO nanocrystals more efficient.

Shortening the processing time is another obvious path for decreasing particle growth. Note in this respect that achieving optimum I_c in BHO-added CC needs faster speed at the nucleation stage (χ_3 in table 2), and hence shorter processing time than in the pristine tape. This is opposite to anticipation, as the optimum processing temperature (χ_1 in table 2) is lower. This may reflect competitiveness of processing goals of achieving good texture while keeping small size of BMO additions. In other words, optimized processing of nanocomposites could be different for templates with different texture sharpness.

Improving the texture sharpness of YBCO in nanocomposites is likely necessary for further optimizing the self-field I_c . It is established that worsening of texture in the nanocomposites is not the effect intrinsic to BMO addition, as 5 mol-% BHO-added PLD-YBCO has the same out-of-plane texture as the pristine YBCO [41]. Moreover, though the texture of BMO-CC is worse than that of pristine tape, the out-of-plane texture of both BHO-CC and BZO-CC is still better (sharper) than that of the LZO template (see table 6). Further studies are necessary to understand the mechanism by which the out-of-plane texture is improved during the process, and why BMO particles inhibit this improvement. Using a nanocrystal-free seed layer as in the study by Li *et al* [43] may help to overcome the

competition between the texture sharpness and nanoparticle coarsening.

Finally, our studies demonstrate that DoE approach appears to be extremely useful. Thus, it is worth repeating this study by optimizing the in-field performance and extend the DoE plan involving other processing parameters. Particularly important could be optimization of oxygenation process, as the low-temperature oxygenation kinetics of BHO-CC and BZO-CCs are much more sluggish than in the pristine CC [37].

5. Conclusion


In this work, we demonstrate the *ex-situ* route for introducing preformed BMO nanocrystals in CSD-YBCO. This technology was successfully transferred from the lab to industrial scale, which required additional process optimization using a DoE approach to reach a moderate (10%–40%) improvement of the in-field performance in BHO-CC compared to pristine CC; the tape speed and the maximum processing temperature at the so-called nucleation step of the heat treatment were shown to be most significant factors.


However, adding BMO nanocrystals as pinning centers in CC was less effective compared to the case when single-crystal substrates were used. Worsening of texture and strong coarsening of BMO nanoparticles were identified as the major obstacles for improving pinning as observed via XRD and TEM measurements. Y dissolution in BMO nanoparticles as one of the possible reasons for coarsening was experimentally confirmed. Also, under the same processing conditions, coarsening of BZO nanoparticles was found to be larger than that of BHO. Future efforts should be directed to understand the mechanism and kinetics of coarsening of BMO nanoparticles to have better control the particle size distribution in combination with good out-of-plane texture of YBCO.


Acknowledgments


The authors thank Markus Hein and Claudia Karbach for characterizing electrical properties of CCs, and Michael Weingärtner for the experiments planning. The authors also thank the whole D-Nano team for their effort on the fabrication of the CCs. We are also grateful to Professor Witzleben (University of Applied Science, Bonn-Rhein-Sieg) for discussing different aspects of XRD analysis using 2D detectors.

ORCID iDs

Hannes Rijckaert  <https://orcid.org/0000-0002-6078-2919>

Jens Hänisch  <https://orcid.org/0000-0003-2757-236X>

Alexander Meledin  <https://orcid.org/0000-0002-3200-0553>

Isabel Van Driessche  <https://orcid.org/0000-0001-5253-3325>

References

- [1] Bäcker M, Baumann A, Brunkahl O, Erbe M and Schneller T 2019 *Chemical Solution Deposition (CSD)* pp 1–34
- [2] Malozemoff A, Annavarapu S, Fritzsche L, Li Q, Prunier V, Rupich M, Thieme C, Zhang W, Goyal A and Paranthaman M 2000 Low-cost YBCO coated conductor technology *Supercond. Sci. Technol.* **13** 473
- [3] Larbalestier D, Gurevich A, Feldmann D M and Polyanskii A 2001 High- T_c superconducting materials for electric power applications *Nature* **414** 368–77
- [4] MacManus-Driscoll J, Foltyn S, Jia Q, Wang H, Serquis A, Civale L, Maiorov B, Hawley M, Maley M and Peterson D 2004 Strongly enhanced current densities in superconducting coated conductors of $\text{YBa}_2\text{Cu}_3\text{O}_{7-x} + \text{BaZrO}_3$ *Nat. Mater.* **3** 439–43
- [5] Matsumoto K and Mele P 2009 Artificial pinning center technology to enhance vortex pinning in YBCO coated conductors *Supercond. Sci. Technol.* **23** 014001
- [6] Obradors X, Puig T, Ricart S, Coll M, Gazquez J, Palau A and Granados X 2012 Growth, nanostructure and vortex pinning in superconducting $\text{YBa}_2\text{Cu}_3\text{O}_7$ thin films based on trifluoroacetate solutions *Supercond. Sci. Technol.* **25** 123001
- [7] Xu A, Delgado L, Khatri N, Liu Y, Selvamanickam V, Abrahimov D, Jaroszynski J, Kametani F and Larbalestier D 2014 Strongly enhanced vortex pinning from 4 to 77 K in magnetic fields up to 31 T in 15 mol.% Zr-added (Gd, Y)-Ba-Cu-O superconducting tapes *APL Mater.* **2** 046111
- [8] Miura M, Yoshizumi M, Izumi T and Shiohara Y 2009 Formation mechanism of BaZrO_3 nanoparticles in $\text{Y}_{1-x}\text{Sm}_x\text{Ba}_2\text{Cu}_3\text{O}_y$ coated conductors derived from trifluoroacetate metal-organic deposition *Supercond. Sci. Technol.* **23** 014013
- [9] Miura M *et al* 2017 Tuning nanoparticle size for enhanced functionality in perovskite thin films deposited by metal organic deposition *NPG Asia Mater.* **9** e447
- [10] Cayado P, Rijckaert H, Erbe M, Langer M, Jung A, Hänisch J and Holzapfel B 2020 CSD-grown $\text{Y}_{1-x}\text{Gd}_x\text{Ba}_2\text{Cu}_3\text{O}_{7-\delta} - \text{BaHfO}_3$ nanocomposite films on Ni5W and IBAD technical substrates *Nanomaterials* **10** 21
- [11] Obradors X, Puig T, Li Z, Pop C, Mundet B, Chamorro N, Vallés F, Coll M, Ricart S and Vallejo B 2018 Epitaxial $\text{YBa}_2\text{Cu}_3\text{O}_{7-x}$ nanocomposite films and coated conductors from BaMO_3 (M=Zr, Hf) colloidal solutions *Supercond. Sci. Technol.* **31** 044001
- [12] Rijckaert H and Van Driessche I 2020 Superconducting $\text{YBa}_2\text{Cu}_3\text{O}_{7-\delta}$ nanocomposite films using preformed ZrO_2 nanocrystals via chemical solution deposition *Superconductivity: From Materials Science to Practical Applications* ed P Mele, K Prassides, C Tarantini, A Palau, P Badica, A K Jha and T Endo (Cham: Springer International Publishing) pp 133–67
- [13] Cayado P, De Keukeleere K, Garzón A, Perez-Mirabet L, Meledin A, De Roo J, Vallés F, Mundet B, Rijckaert H and Pollefeyt G 2015 Epitaxial $\text{YBa}_2\text{Cu}_3\text{O}_{7-x}$ nanocomposite thin films from colloidal solutions *Supercond. Sci. Technol.* **28** 124007
- [14] Bretos I, Schneller T, Falter M, Bäcker M, Hollmann E, Wördenweber R, Molina-Luna L, Van Tendeloo G and Eibl O 2015 Solution-derived $\text{YBa}_2\text{Cu}_3\text{O}_{7-\delta}$ (YBCO) superconducting films with BaZrO_3 (BZO) nanodots based on reverse micelle stabilized nanoparticles *J. Mater. Chem.* **3** 3971–9
- [15] De Keukeleere K *et al* 2016 Superconducting $\text{YBa}_2\text{Cu}_3\text{O}_{7-\delta}$ nanocomposites using preformed ZrO_2 nanocrystals: growth mechanisms and vortex pinning properties *Adv. Electr. Mater.* **2** 1600161
- [16] Rijckaert H, Pollefeyt G, Sieger M, Hänisch J, Bennowitz J, De Keukeleere K, De Roo J, Hühne R, Bäcker M and Paturi P 2017 Optimizing nanocomposites through nanocrystal surface chemistry: superconducting $\text{YBa}_2\text{Cu}_3\text{O}_7$ thin films via low-fluorine metal organic deposition and preformed metal oxide nanocrystals *Chem. Mater.* **29** 6104–13
- [17] Rijckaert H, Cayado P, Nast R, Diez Sierra J, Erbe M, López Domínguez P, Hänisch J, De Buysser K, Holzapfel B and Van Driessche I 2020 Superconducting HfO_2 - $\text{YBa}_2\text{Cu}_3\text{O}_{7-\delta}$ nanocomposite films deposited using ink-jet printing of colloidal solutions *Coatings* **10** 17
- [18] Li Z, Coll M, Mundet B, Chamorro N, Vallés F, Palau A, Gazquez J, Ricart S, Puig T and Obradors X 2019 Control of nanostructure and pinning properties in solution deposited $\text{YBa}_2\text{Cu}_3\text{O}_{7-x}$ nanocomposites with preformed perovskite nanoparticles *Sci. Rep.* **9** 5828
- [19] Diez Sierra J, Lopez-Dominguez P, Rijckaert H, Rikel M O, Hänisch J, Khan M Z, Falter M, Bennowitz J, Huhtinen H and Schäfer S 2020 High critical current density and enhanced pinning in superconducting films of $\text{YBa}_2\text{Cu}_3\text{O}_{7-\delta}$ nanocomposites with embedded BaZrO_3 , BaHfO_3 , BaTiO_3 and SrZrO_3 nanocrystals *ACS Appl. Nano Mater.* **3** 5542–53
- [20] López-Domínguez P 2020 *et al* Process for producing nanoparticles WO 2020 049019 A1
- [21] Rijckaert H, De Roo J, Van Zele M, Banerjee S, Huhtinen H, Paturi P, Bennowitz J, Billinge S, Bäcker M and De Buysser K 2018 Pair distribution function analysis of ZrO_2 nanocrystals and insights in the formation of ZrO_2 - $\text{YBa}_2\text{Cu}_3\text{O}_7$ nanocomposites *Materials* **11** 1066
- [22] Bäcker M, Falter M, Brunkahl O and Holzapfel B 2013 Superconducting films *Chemical Solution Deposition of Functional Oxide Thin Films* ed T Schneller, R Waser, M Kosec and D Payne (Berlin: Springer) pp 673–705
- [23] Witte M, Gottstein G, De Boer N, Gilges S, Klöwer J, Bäcker M, Brunkahl O, Wojtyniak B, Mader W and Svete M 2014 The project SupraMetall: towards commercial fabrication of high-temperature superconducting tapes *Adv. Eng. Mater.* **16** 539–49
- [24] Bäcker M, Feenstra R, Mosiadz M, Wojtyniak B, Kunert J, Brunkahl O, Rikel M, Falter M and Sadewasser M 2019 Industrial scale 40mm production technology at D-Nano *European Conf. Applied Superconductivity (Glasgow)*
- [25] Feenstra R, Sadewasser M and Bäcker M 2016 Process for the production of high temperature superconductor wires WO 2016/150781
- [26] Rijckaert H, Hänisch J, Pollefeyt G, Bäcker M and Van Driessche I 2019 Influence of Ba^{2+} consumption and intermediate dwelling during processing of $\text{YBa}_2\text{Cu}_3\text{O}_7$ nanocomposite films *J. Am. Ceram. Soc.* **102** 3870–8

- [27] Brereton R G 2003 *Chemometrics: Data Analysis for the Laboratory and Chemical Plant* (New York: Wiley)
- [28] Yücel E, Güler N and Yücel Y 2014 Optimization of deposition conditions of CdS thin films using response surface methodology *J. Alloys Compd.* **589** 207–12
- [29] Strickland N, Hoffmann C and Wimbush S 2014 A 1 kA-class cryogen-free critical current characterization system for superconducting coated conductors *Rev. Sci. Instrum.* **85** 113907
- [30] Scardi P, Leoni M and Delhez R 2004 Line broadening analysis using integral breadth methods: a critical review *J. Appl. Crystallogr.* **37** 381–90
- [31] Specht E, Goyal A, Lee D, List F, Kroeger D, Paranthaman M, Williams R and Christen D 1998 Cube-textured nickel substrates for high-temperature superconductors *Supercond. Sci. Technol.* **11** 945
- [32] Rikel M O, Isfort D, Klein M, Ehrenberg J, Bock J, Specht E D, Sun-Wagener M, Weber O, Sporn D and Engel S 2009 Simplified procedure for estimating epitaxy of $\text{La}_2\text{Zr}_2\text{O}_7$ -buffered NiW RABITS using XRD *IEEE Trans. Appl. Supercond.* **19** 3307–10
- [33] Rikel M, Ehrenberg J, Mahachi S, Klein M, Hoppe B, Schutz J and Bock J 2010 Development of all-CSD processes for coated conductors at Nexans: limitations and possible solutions *IEEE Trans. Appl. Supercond.* **21** 2928–32
- [34] Kovács A, Schierholz R and Tillmann K 2016 FEI Titan G2 80–200 CREWLEY *JLSRF* **2** 43
- [35] Koblishka-Veneva A, Sakai N, Tajima S and Murakami M 2003 *YBCO Handbook of Superconducting Materials* vol 1, ed D A Cardwell and D S Ginley (Boca Raton, FL: CRC Press) 2085
- [36] Jorgensen J D, Hinks D, Radaelli P, Pei S, Lightfoot P, Dabrowski B, Segre C and Hunter B 1991 Defects, defect ordering, structural coherence and superconductivity in the 123 copper oxides *Physica C* **185** 184–9
- [37] Diez Sierra J, Rikel M, Rijckaert H, Falter M, Khan M, Huhtinen H, Paturi P, Bäcker M and Van Driessche I 2019 Oxygen doping effects in CSD-YBCO nanocomposite films with preformed nanocrystals *EUCAS 2019*
- [38] Rijckaert H, Cayado P, Hanisch J, Billet J, Erbe M, Holzapfel B and Van Driessche I 2021 Unravelling the crystallization process in solution-derived $\text{YBa}_2\text{Cu}_3\text{O}_{7-\delta}$ nanocomposite films with preformed ZrO_2 nanocrystals via definitive screening design *J. Phys. Chem. Lett.* **12** 2118–25
- [39] Willa R, Koshelev A E, Sadovskyy I A and Glatz A 2017 Strong-pinning regimes by spherical inclusions in anisotropic type-II superconductors *Supercond. Sci. Technol.* **31** 014001
- [40] Reich E, Thersleff T, Hühne R, Iida K, Schultz L and Holzapfel B 2009 Structural and pinning properties of $\text{Y}_2\text{Ba}_4\text{CuMO}_y$ ($M=\text{Nb, Zr}$)/ $\text{YBa}_2\text{Cu}_3\text{O}_{7-\delta}$ quasi-multilayers fabricated by off-axis pulsed laser deposition *Supercond. Sci. Technol.* **22** 105004
- [41] Sieger M, Hänisch J, Pahlke P, Sparing M, Gaitzsch U, Iida K, Nast R, Reich E, Schultz L and Holzapfel B 2015 BaHfO_3 -doped thick $\text{YBa}_2\text{Cu}_3\text{O}_{7-\delta}$ films on highly alloyed textured Ni-W tapes *IEEE Trans. Appl. Supercond.* **25** 1–4
- [42] Majkic G *et al* 2020 Strain equilibrium, chemical configuration and defect chemistry of the REBCO/BZO nanorod system of high-performance REBCO tapes *Presentation at ASC2020*
- [43] Imashuku S, Uda T, Nose Y and Awakura Y 2010 To journal of equilibria and diffusion phase relationship of the $\text{BaO-ZrO}_2\text{-YO}_{1.5}$ system at 1500 and 1600 °C *J. Phase Equilib. Diffus.* **31** 348–56
- [44] Kato K, Han D and Uda T 2019 Transport properties of proton conductive Y-doped BaHfO_3 and Ca or Sr-substituted Y-doped BaZrO_3 *J. Am. Ceram. Soc.* **102** 1201–10
- [45] Gonçalves M, Maram P, Muccillo R and Navrotsky A 2014 Enthalpy of formation and thermodynamic insights into yttrium doped BaZrO_3 *J. Mater. Chem. A* **2** 17840–7
- [46] Wesolowski D, Patta Y and Cima M 2009 Conversion behavior comparison of TFA-MOD and non-fluorine solution-deposited YBCO films *Physica C* **469** 766–73
- [47] Baldan A 2002 Review progress in Ostwald ripening theories and their applications to nickel-base superalloys Part I: Ostwald ripening theories *J. Mater. Sci* **37** 2171–202
- [48] Haugan T, Barnes P, Wheeler R, Meisenkothen F and Sumption M 2004 Addition of nanoparticle dispersions to enhance flux pinning of the $\text{YBa}_2\text{Cu}_3\text{O}_{7-x}$ superconductor *Nature* **430** 867–70

Repository KITopen

Dies ist ein Postprint/begutachtetes Manuskript.

Empfohlene Zitierung:

Díez-Sierra, J.; Rijckaert, H.; Rikel, M.; Hänisch, J.; Sadewasser, M.; Koliotassis, L.; Meledin, A.; López-Domínguez, P.; Falter, M.; Bennewitz, J.; Bäcker, M.; Driessche, I. V.
All-chemical YBa₂Cu₃O_{7-δ} coated conductors with preformed BaHfO₃ and BaZrO₃ nanocrystals on Ni₅W technical substrate at the industrial scale.
2021. Superconductor science and technology, 34
doi: [10.554/IR/1000141056](https://doi.org/10.554/IR/1000141056)

Zitierung der Originalveröffentlichung:

Díez-Sierra, J.; Rijckaert, H.; Rikel, M.; Hänisch, J.; Sadewasser, M.; Koliotassis, L.; Meledin, A.; López-Domínguez, P.; Falter, M.; Bennewitz, J.; Bäcker, M.; Driessche, I. V.
All-chemical YBa₂Cu₃O_{7-δ} coated conductors with preformed BaHfO₃ and BaZrO₃ nanocrystals on Ni₅W technical substrate at the industrial scale.
2021. Superconductor science and technology, 34 (11), 114001.
doi:[10.1088/1361-6668/ac2495](https://doi.org/10.1088/1361-6668/ac2495)

Lizenzinformationen: CC BY-NC-ND 4.0